Journal of Materials Chemistry C

ROYAL SOCIETY OF CHEMISTRY

COMMUNICATION

View Article Online
View Journal | View Issue

Cite this: J. Mater. Chem. C, 2024, 12, 13809

Received 16th May 2024,
Accepted 16th August 2024

DOI: 10.1039/d4tc02030h

rsc.li/materials-c

Epitaxially grown single-crystalline $SrTiO_3$ membranes using a solution-processed, amorphous $SrCa_2Al_2O_6$ sacrificial layer†

Shivasheesh Varshney, *[a] Martí Ramis, [b] Sooho Choo,[a] Mariona Coll [b] and Bharat Jalan *[a]

Water-soluble sacrificial layers based on epitaxially grown, single crystalline (Ca, Sr, Ba)$_3Al_2O_6$ layers are widely used for creating free-standing perovskite oxide membranes. However, obtaining these sacrificial layers with intricate stoichiometry remains a challenge, especially for molecular beam epitaxy (MBE). In this study, we demonstrate the hybrid MBE growth of epitaxial, single crystalline $SrTiO_3$ films using a solution processed, amorphous $SrCa_2Al_2O_6$ sacrificial layer onto $SrTiO_3$ (001) substrates. Prior to the growth, oxygen plasma exposure was used to first create the crystalline $SrCa_2Al_2O_6$ layer with well-defined surface crystallinity. Utilizing reflection high energy electron diffraction, X-ray diffraction, and atomic force microscopy, we observe an atomic layer-by-layer growth of epitaxial, single crystalline $SrTiO_3$ films on the $SrCa_2Al_2O_6$ layer with atomically smooth surfaces. The $SrCa_2Al_2O_6$ layer was subsequently dissolved in deionized water to create free-standing $SrTiO_3$ membranes that were transferred onto a metal-coated Si wafer. Membranes created with Sr-deficiency revealed ferroelectric-like behavior measured using piezo-force microscopy whereas stoichiometric films retained paraelectric-like behavior. These findings underscore the viability of using *ex situ* deposited amorphous $SrCa_2Al_2O_6$ for epitaxial, single crystalline growth, as well as the importance of point defects in determining the ferroic properties in membranes.

Introduction

Free-standing oxide membranes have garnered significant interest due to their usefulness in strain- or strain-gradient engineering, moiré engineering, and artificial heterostructure engineering.[1–8] These capabilities help to tailor the properties such as superconductivity, magnetoresistance, ferroelectricity, metal–insulator transitions, and numerous others.[9–17] A common method to fabricate a free-standing membrane involves the use of chemically etchable sacrificial layers.[15–21] These sacrificial layers enable the release of a functional film from the growth substrate through selective etching, without causing damage to the film. This method results in the synthesis of millimeter-sized membranes.[15–21] This technique also promotes the reuse of expensive single crystal substrates following film exfoliation.

Epitaxially grown, single-crystalline $Sr_3Al_2O_6$, alloyed with $Ca_3Al_2O_6$ and/or $Ba_3Al_2O_6$, has found widespread use as a sacrificial layer in pulsed laser deposition (PLD) techniques.[9,16,22] $Sr_3Al_2O_6$ possesses a pseudocubic perovskite structure, with a cubic unit cell having a lattice parameter of 15.844 Å (÷ 4 = 3.961 Å). The (Ba, Sr, Ca)$_3Al_2O_6$ system allows for continuous adjustment of the lattice parameter within the range of 3.816–4.125 Å, a range frequently observed in typical perovskite oxides (3.8–4.1Å). Moreover, the electronegativity of these alkaline-earth metals affects the solubility of sacrificial layers in water, decreasing in the order of increasing electronegativity (Ba^{2+} < Sr^{2+} < Ca^{2+}).[23,24] Among these solid-solutions, $SrCa_2Al_2O_6$, with a lattice parameter of 3.86 Å, has been used for perovskite growth in PLD studies.[9]

An alternative to PLD, chemical solution deposition (CSD), has also been investigated to create amorphous $SrCa_2Al_2O_6$ layers.[23] CSD is a versatile method to synthesize ternary and quaternary oxides, which can deliver low-cost production in broad applications.[25–28] The method exploits engineering solution-precursor chemistry to achieve the (Sr, Ca)$_3Al_2O_6$ composition on single-crystal substrates.[23,24] It involves three steps: first, stabilization of precursor solution and then homogeneous deposition by spin coating, followed by thermal annealing to convert precursor gels to phase pure, epitaxial films.[23] In the past, PLD growth of $La_{0.7}Sr_{0.3}MnO_3$ (LSMO) films having a surface roughness of about 2 nm has been explored on solution-deposited (Ba, Sr, Ca)$_3Al_2O_6$ sacrificial layers.[24] However, the growth of such sacrificial layers with complex stoichiometry is not straightforward in molecular beam epitaxy (MBE). Furthermore, the low

[a] Department of Chemical Engineering and Materials Science, University of Minnesota, Twin Cities, Minnesota, 55455, USA. E-mail: varsh022@umn.edu, bjalan@umn.edu

[b] ICMAB-CSIC, Campus UAB 08193, Bellaterra, Barcelona, Spain

† Electronic supplementary information (ESI) available. See DOI: https://doi.org/10.1039/d4tc02030h

vapor pressure and acceptor-like behavior of some elements such as Al (acting as a deep-acceptor in $SrTiO_3$ (STO)) can prohibit their use in oxide MBE. This is evident by the fact that as of 2023, only a small fraction, approximately one-tenth, of all publications (70+) employed MBE for oxide membrane growth.[29] Varshney *et al.*[29] have recently introduced a novel approach suitable for MBE, involving the use of binary alkaline-earth oxide sacrificial layers. These layers are conducive to MBE processes, as alkaline-earth metals can be sublimated at temperatures ranging from 300 to 500 °C and readily oxidize in molecular oxygen to form the corresponding oxides. Additionally, the binary oxide sacrificial layer (Mg, Ca, Sr, Ba)O provides a wide range of lattice parameter tuning capabilities and faster dissolution (<5 minutes).[29] When combined with complex sacrificial layers, they allow continuous tuning of lattice parameters from 2.98 to 5.12 Å.[29]

One approach to incorporate complex sacrificial layers in MBE processes is to prepare them *ex situ* and subsequently utilize them as substrates for film growth *via* MBE. In this study, we grow epitaxial single crystalline STO using hybrid MBE on CSD synthesized, amorphous $SrCa_2Al_2O_6$ sacrificial layers. We first show recrystallization of air-exposed amorphous $SrCa_2Al_2O_6$ into a single crystalline, epitaxial film. This recovery of the surface crystal structure is possible even after 365+ days of $SrCa_2Al_2O_6$ sample preparation. We show layer-by-layer growth of the STO film with an atomically smooth surface having a roughness of ~0.223 nm. We show exfoliation and transfer of membranes to other substrates followed by structural characterization using X-ray diffraction. The transferred membranes further show an atomically smooth surface with a roughness of 0.268 nm and a bulk-like lattice parameter. We characterize the electrical properties of membranes using piezo-force microscopy (PFM). Our characterization reveals ferroelectric-like switching and hysteresis loops in Sr-deficient membranes.

Experiment

$SrCa_2Al_2O_6$ composition was prepared on a single crystalline STO (001) substrate using the CSD method, employing a metal nitrate precursor route as shown in Fig. 1a. The precursor solution was prepared for $SrCa_2Al_2O_6$ using stoichiometric amounts of $Sr(NO_3)_2$ strontium nitrate (>99%), $Ca(NO_3)_2$ calcium nitrate (>99%), and $Al(NO_3)_3{\cdot}9H_2O$ hydrated aluminum nitrate (>98%), which were dissolved in Milli-Q water with citric acid $C_6H_8O_7$ (>99%) to obtain 0.1 M solution. Further details are discussed elsewhere.[23] This solution was spin coated to obtain a 20 nm thick $SrCa_2Al_2O_6$ film on the STO substrate and was annealed in an oxygen furnace for 1 hour at 900 °C prior to being sealed in air in a plastic bag as

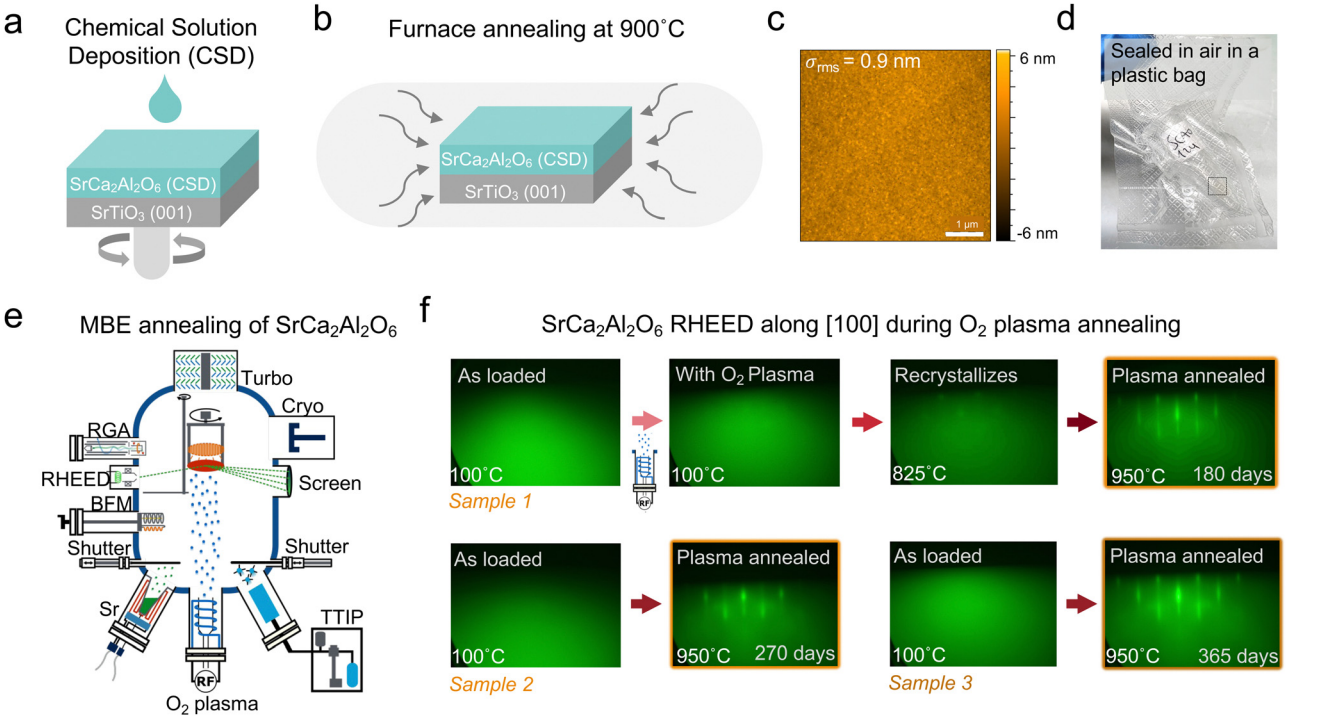

Fig. 1 Synthesis process illustrating a way to obtain epitaxial, single crystalline $SrCa_2Al_2O_6$ films from a solution-grown amorphous $SrCa_2Al_2O_6$ layer on the $SrTiO_3$ substrate. (a) Schematic illustration of the chemical solution deposition (CSD) method of $SrCa_2Al_2O_6$ sacrificial on STO (001). (b) The as-prepared $SrCa_2Al_2O_6$/STO (001) is oxygen annealed at 900 °C. (c) The AFM image of $SrCa_2Al_2O_6$ after furnace annealing showing a smooth surface with an rms roughness of ~0.9 nm. (d) Picture of the plastic bag, where the as-prepared $SrCa_2Al_2O_6$ after annealing was sealed in air. (e) Schematic of the hybrid MBE system for vacuum annealing of the as-prepared samples with oxygen (O_2) plasma. (f) RHEED evolution during plasma annealing of $SrCa_2Al_2O_6$ on the STO (001) substrate. The as-loaded sample 1 is amorphous at 100 °C. As soon as O_2 plasma starts, the sample shows spots in RHEED, indicating crystallinity. As temperature increases, $SrCa_2Al_2O_6$ crystallizes. The RHEED image at 950 °C shows that $SrCa_2Al_2O_6$ is epitaxial on the STO substrate. This recovery of RHEED is possible even after 270 days (sample 2) and 365 days (sample 3) of $SrCa_2Al_2O_6$ sample preparation.

shown in Fig. 1b–d. The $SrCa_2Al_2O_6$ samples exposed to air inside the plastic bag for up to ~180, 270, and 365 days were loaded into the load lock of the MBE chamber (Scienta Omicron Inc.). The moisture in the load lock that entered during loading of the sample was removed by baking the chamber for 2 hours at 150 °C. A base pressure of 3×10^{-9} torr was achieved after lamp heating the load lock. The sample was then transported *in situ* to the MBE growth chamber, which has a base pressure of 5×10^{-9} torr. Reflection high-energy electron diffraction (RHEED) (Staib Instruments) was used to determine the surface crystallinity of the as-loaded sample. A radio-frequency (RF) oxygen plasma source operated at 250 W at an oxygen pressure of 8×10^{-6} torr was used for annealing while the sample was ramped up to 950 °C (at 25 °C min^{-1} until 650 °C and 10 °C min^{-1} from 650 to 950 °C). The sample was annealed at 950 °C for 20 min prior to the growth. A four unit-cell of the seed layer of STO was grown on $SrCa_2Al_2O_6$ at 950 °C using a hybrid MBE approach,[30] by co-deposition of Sr (99.99% Sigma Aldrich), titanium tetraisopropoxide (TTIP) 99.999% Sigma Aldrich, and oxygen plasma. Subsequently, the sample was annealed again under oxygen plasma for 20 min before restarting the growth of the final STO layer. It should be noted that the TTIP precursor was supplied using a gas inlet system consisting of a linear leak valve and a Baratron monometer.[30] The Sr beam equivalent pressure (BEP) was fixed at 7.7×10^{-8} torr, oxygen plasma at 250 W and an oxygen pressure of 5×10^{-6} torr. Tuning TTIP BEP allowed changing stoichiometry in the STO film. *Ex situ* surface characterization using atomic force microscopy (AFM) in a peak-force mode was performed to check the surface morphology and high-resolution X-ray diffraction (HRXRD) was performed using a Rigaku SmartLab XE thin film diffractometer equipped with Cu Kα radiation. XRD measurements were used to examine the phase purity, crystallinity, and out-of-plane lattice parameter. The thickness of STO films was measured using grazing incidence X-ray reflectivity (GIXR) with data fitted using the GenX software.

For exfoliation, a polydimethylsiloxane (PDMS) supporting layer was applied on top of the STO/$SrCa_2Al_2O_6$/STO (001) sample. The top surface of the heterostructure adheres to the PDMS stamp. The sample is subsequently placed in deionized water at room temperature for 4–5 days to ensure complete dissolution of the $SrCa_2Al_2O_6$ sacrificial layer. After dissolution, the STO substrate was detached from the PDMS/STO structure. The PDMS stamp with the STO membrane was then applied to the Au-coated Si substrate placed on a hot plate at 120 °C for 5 min. PDMS was gently peeled off resulting in the transfer of the membrane on the Au-coated Si substrate. HRXRD and AFM were used to characterize the transferred membrane. Piezo-force microscopy (PFM), Bruker NanoScope V Dimension Icon equipped with a generic lock-in amplifier, was used to measure the piezo response of the membranes in the PFM optimized vertical domain operation module. Pt-coated Ir cantilevers (SCM-PIT-V2 sample, l = 225 μm, resonant frequency = 75 kHz, and spring constant k = 3 N m^{-1}) were used for tapping mode AFM measurements, in which vertical deflection was set to zero, and a laser sum signal was set to 4.5–5 V. The sample was grounded with a carbon tape, where the Au-coated Si substrate acted as the bottom electrode. Measurements were performed using a tip in a tapping mode with the top surface of the membrane and a bias applied through the tip. The box-like switching scans were performed, and the sample surface was polled by ±10 volts tip bias and scanned using a tip at 0 V after 30 minutes of polling the sample. In PFM, a drive frequency of 72.15208 kHz and a drive amplitude of 10 000 mV were used for the measurement. Furthermore, switching spectroscopy was performed using voltage pulse sequence sweeping (positive to negative waveforms) as illustrated here[31] to obtain the bias dependence of the PFM phase and amplitude.

Results and discussion

Fig. 1 shows the process employed to obtain the crystalline 20 nm $SrCa_2Al_2O_6$ layer on the STO (001) substrate. First, solution processing (CSD) is used to deposit $SrCa_2Al_2O_6$ (Fig. 1a). To improve the crystallinity, the as-prepared $SrCa_2Al_2O_6$/STO (001) undergoes an optimized thermal treatment in a tubular furnace at 900 °C for 30 min at a heating/cooling rate of 25 °C min^{-1} and an O_2 flow of 0.6 L min^{-1} as shown in Fig. 1b. AFM of the as-prepared sample shows a surface roughness of ~0.9 nm (Fig. 1c). This 900 °C annealing step is necessary for the decomposition of metal nitrate precursor solution and crystallization of the stoichiometric $SrCa_2Al_2O_6$ layer.[23] The $SrCa_2Al_2O_6$/STO sample is subsequently sealed in air in a plastic bag[24] for storage and transportation to the MBE system (Fig. 1d). This step is important to reduce potential degradation of the $SrCa_2Al_2O_6$ sample. The plastic bag containing samples was stored in a controlled environment in a N_2 filled desiccator. Although the samples were sealed in a plastic bag to control air exposure during transport, they still turned amorphous. Fig. 1e shows a schematic of the MBE chamber, where the $SrCa_2Al_2O_6$/STO sample is loaded for the STO growth after ~180, 270, and 365 days of its preparation. The RHEED image of the as-loaded sample shows an amorphous film, which starts to recrystallize as the substrate temperature is increased from 100 °C to 950 °C in the presence of oxygen plasma (Fig. S1, ESI†). Fig. 1f shows RHEED images during annealing under oxygen plasma at select temperatures for three different samples. A clear streaky RHEED pattern of $SrCa_2Al_2O_6$ is observed at 950 °C, which indicates the epitaxial, single crystalline film on the STO (001) surface. While the crystallization mechanism is unclear, it is noteworthy that the oxygen plasma annealing not only cleans up the surface but also helps to achieve single crystallinity. A similar result using the vacuum annealing in the PLD chamber was reported earlier.[32] Furthermore, it is remarkable that $SrCa_2Al_2O_6$ films turn epitaxial and single crystalline even after ~180 (sample 1), 270 (sample 2), and 365 (sample 3) days of preparation using the CSD method (Fig. 1f).

Fig. 2a shows the RHEED intensity oscillations during STO growth as a function of time during growth indicating an atomic layer-by-layer growth mode. The growth rate calculated from the RHEED oscillations is 1.73 nm min^{-1}, thus giving a

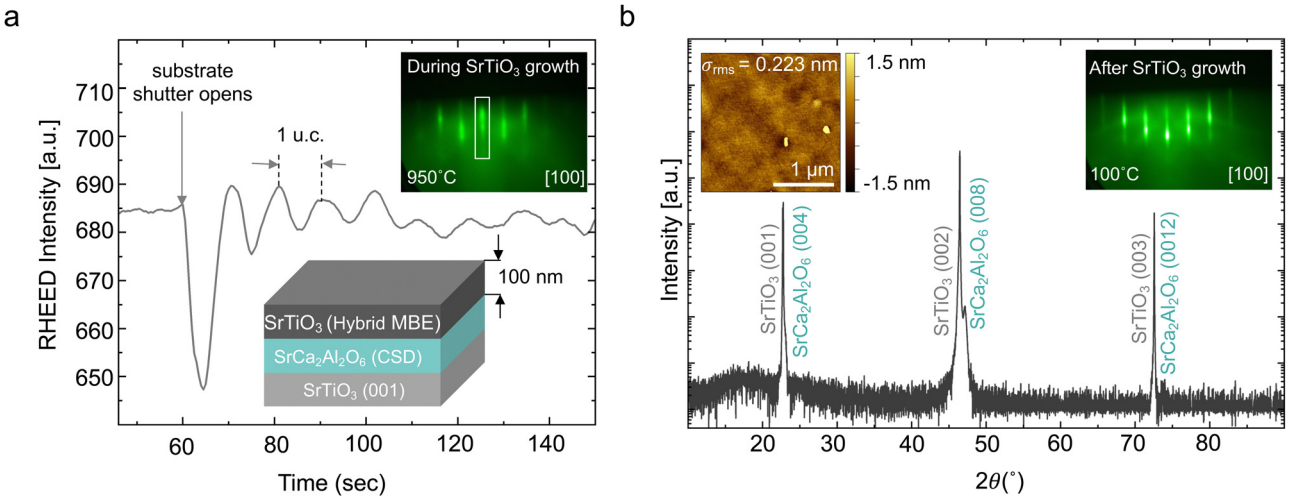

Fig. 2 Epitaxial single-crystalline growth of STO on the $SrCa_2Al_2O_6$/STO (001) substrate. (a) RHEED intensity oscillations during STO growth, indicating an atomic layer-by-layer growth mode. The inset shows a sample schematic and RHEED image taken during growth at 950 °C. The intensity profile is shown for the RHEED spot within a box. (b) A 2θ–ω coupled scan of 104 nm STO/20 nm on the $SrCa_2Al_2O_6$/STO (001) substrate, indicating single-crystalline, phase-pure, stoichiometric STO films. The inset shows the RHEED image after STO growth and the AFM image of STO with a rms roughness of 0.223 nm.

film thickness of 104 nm for 1 hour of growth. The RHEED images shown in the inset of Fig. 2a show streaky patterns indicating an epitaxial film with a smooth surface. It is important to note that the RHEED oscillations were observed only when a 4 unit-cell of STO/$SrCa_2Al_2O_6$/STO (001) was grown and annealed. No oscillations were observed if the STO seed layer was not used (Fig. S2a, ESI†). However, the STO films without the seed layer also remain epitaxial and single crystalline, as observed by RHEED (Fig. S2b and c, ESI†). The 2θ–ω coupled scan shows phase-pure and single crystalline STO films (Fig. 2b). The out-of-plane lattice parameter extracted from the (002) peak of STO is 3.905 ± 0.002 Å (identical to the bulk) and from the (008) peak of $SrCa_2Al_2O_6$ is 15.39 ± 0.002 Å (÷4 = 3.849 Å), indicating a stoichiometry of $Sr_{0.9}Ca_{2.1}Al_2O_6$ (assuming a relaxed lattice parameter). The bulk-like lattice parameter indicates that the STO film is nearly stoichiometric. We recognize that lattice parameters can be influenced by both stoichiometry and strain relaxation. However, since these films were grown within the MBE growth window,[33,34] the bulk-like lattice parameter indicates a stoichiometric composition and complete strain relaxation.

The inset of Fig. 2b shows an AFM image revealing that the surface is atomically smooth with a surface roughness of 0.223 nm. The RHEED image (inset of Fig. 2b) taken after growth confirms the epitaxial film. Non-stoichiometric (Sr-deficient) STO films were grown on the $SrCa_2Al_2O_6$ layer under the excess of TTIP. A peak shift was observed in the 2θ–ω coupled scan due to non-stoichiometry indicating a lattice parameter of 3.936 ± 0.002 Å and the RHEED image reveals an additional half order diffraction (Fig. S3a–c, ESI†). Furthermore, the GIXR of the stoichiometric film shows a film thickness of 104 nm (Fig. S3c, ESI†), in agreement with the expected layer thickness that is calculated from RHEED intensity oscillations.

Fig. 3a shows the schematic illustration of the exfoliation and transfer process combined with structural characterization. The entire 5 × 5 mm membrane was exfoliated as shown in the inset of Fig. 3a. An uncracked area (>100 μm^2) was transferred onto the Au-coated Si substrate. Fig. 3b shows a wide angle 2θ–ω coupled scan of the transferred membrane revealing the STO film peaks, Au peaks, and Si peaks. No $SrCa_2Al_2O_6$ peaks were observed. Fine coupled scans (Fig. 3c) reveal the Sr-deficient membrane with a lattice parameter of 3.912 ± 0.002 Å and a nominally stoichiometric membrane with a lattice parameter of 3.905 ± 0.002 Å. Additionally, the Sr-deficient film exhibits an asymmetric peak, which is likely attributed to non-stoichiometry rather than strain relaxation. Although these thick membranes are nominally fully relaxed after being separated from the sacrificial layer—as indicated by the shift in the out-of-plane lattice parameter towards the bulk in membranes transferred to an Au-coated Si substrate—the contribution of macroscopic strain, such as wrinkles in the membranes, to the observed asymmetry cannot be entirely ruled out. The full-width at half maximum (FWHM) of the rocking curve around the STO (002) peak reveals that FWHM increases to 1.40° in the transferred membrane as compared to 0.46° in the as-grown film (Fig. S4, ESI†). This increase could be due to a macroscopic disorder in the transferred membrane, arising from wrinkles and/or air-bubbles.

Finally, to probe the dielectric response of these STO membranes, we used PFM and performed box-like switching and hysteresis loop measurements. As shown in Fig. 4, we first applied −10 V over the 4 × 4 μm^2 area and then +10 V over the 2 × 2 μm^2 area. Finally, the 7 × 7 μm^2 area was scanned with 0 V tip bias. A box-like pattern with 180° phase contrast was obtained on the Sr-deficient membrane (Fig. 4a), whereas no phase contrast was observed in the stoichiometric sample (Fig. 4c) when the exact same polling process is performed.

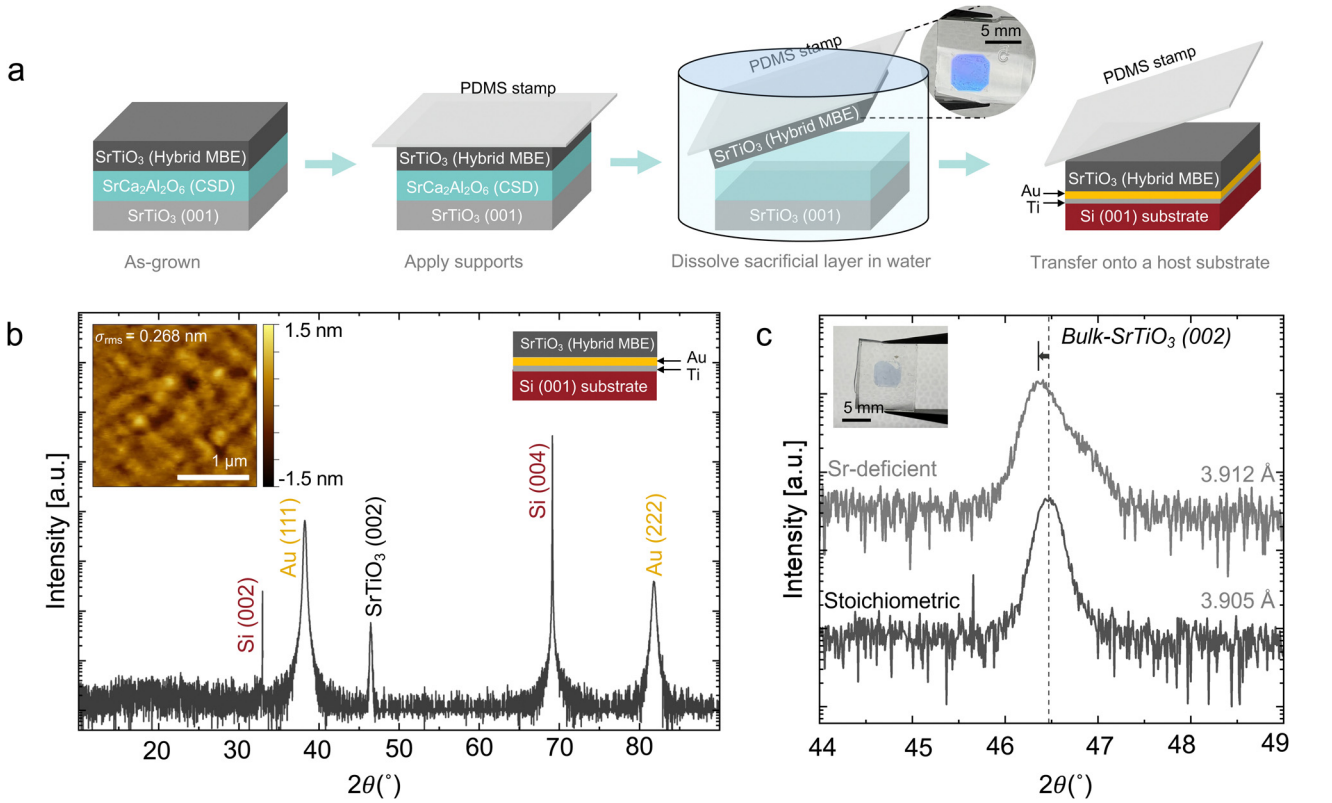

Fig. 3 Exfoliation and transfer of STO membranes to Au-coated Si substrates. (a) Schematic illustration of the process used for exfoliation and transfer of STO membranes onto a host substrate. The inset shows the stoichiometric membrane on the PDMS stamp. (b) A 2θ–ω coupled scan of 104 nm STO on the Au-coated Si substrate. The insets show the AFM image of the transferred membrane and a sample schematic. (c) A fine coupled 2θ–ω scan around the STO (002) peak indicating the stoichiometric membrane with a bulk-like lattice parameter of 3.905 ± 0.002 Å, and a slightly Sr-deficient film with a lattice parameter of 3.912 ± 0.002 Å. The inset shows the Sr-deficient membrane on the PDMS stamp.

Nearly no phase contrast was seen in the region polled at +10 V and unpolled region (*i.e.* +0 V region). The 7 × 7 μm^2 area with 0 V shows the nominal phase and amplitude present in the pristine sample without any polling process. A contrast in amplitude was also observed in the Sr-deficient membrane (Fig. S6c and d, ESI†) and the surface topography remained smooth during the AFM scan. A similar contrast was observed in amplitude and phase when scans were performed at other places over the same Sr-deficient membrane (Fig. S5, ESI†). Phase and amplitude hysteresis loops were obtained on the Sr-deficient membrane (Fig. 4b and Fig. S6a, ESI†) by landing the tip on top of the sample and performing ramp and shoot measurements by modulating the d.c. bias from −12 to 12 V. A local hysteresis loop was obtained on the sample surface

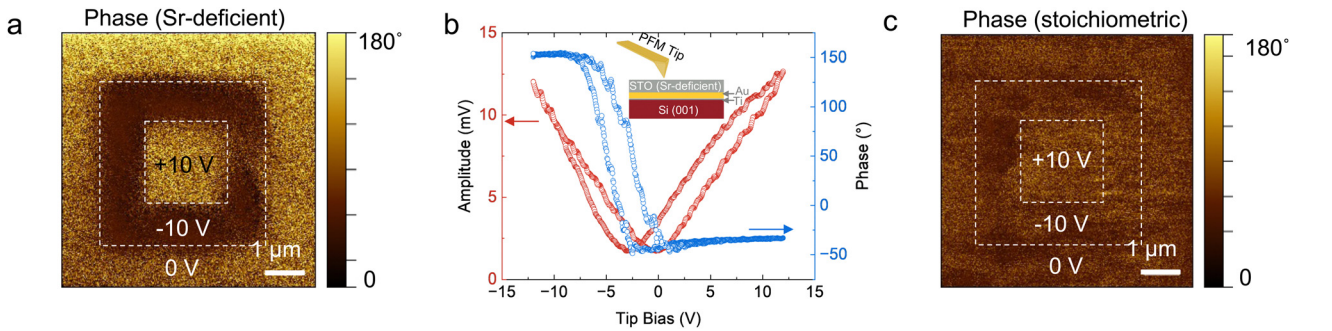

Fig. 4 PFM measurements for Sr-deficient and stoichiometric STO membranes. (a) Phase contrast on applying ±10 V d.c. bias to the tip for the Sr-deficient sample. A 4 × 4 μm^2 area was scanned with −10 V, then a 2 × 2 μm^2 area with +10 V, and finally a 7 × 7 μm^2 area was scanned with 0 V. This result shows polling of sample with the ±10 V bias and pristine state of sample under 0 V bias. (b) PFM phase and amplitude loops taken at the region that was polled to −10 V, showing hysteretic behavior of the Sr-deficient membrane. The inset shows a sample schematic the (c) PFM phase with an application of ±10 V d.c. bias to the tip for the stoichiometric STO sample showing no contrast, when the exact same polling process was performed as in panel (a).

polled to −10 V (Fig. 4b), demonstrating polarization switching behavior. These results indicate room-temperature ferroelectric-like behavior in STO and are consistent with properties commonly observed in Sr-deficient STO thin films.[35–37] STO, being an incipient ferroelectric, can show ferroelectric properties under strain, or stoichiometry deviations, electric field, and alloying with (Ca, Ba).[38–43]

Conclusions

In summary, we have demonstrated that the CSD-grown sacrificial layer of $SrCa_2Al_2O_6$ can be transformed using high temperature, oxygen plasma annealing from an amorphous state to an epitaxial single crystalline film even after 365 days of exposure to air. An atomically smooth, phase pure, epitaxial STO film was subsequently grown on $SrCa_2Al_2O_6$ using hybrid MBE. The sacrificial layer is dissolved to exfoliate millimeter-sized membranes, which are transferred on to the Au-coated Si substrate. The membranes show bulk-like structural properties with an atomically smooth surface. Furthermore, we demonstrate ferroelectric-like behavior in Sr-deficient STO membranes using PFM. Our results highlight a facile method to fabricate membranes using CSD by tackling the challenge to grow complicated stoichiometry of $SrCa_2Al_2O_6$ in MBE, and yet using MBE to grow single crystal functional oxide membranes. This work combines two powerful techniques (CSD of $SrCa_2Al_2O_6$ and hybrid MBE for STO) for the synthesis. Our study broadens the platform of the synthesis of sacrificial layers and functional membranes, thus creating new opportunities and applications in science and engineering.

Author contributions

S. V. and B. J. conceived the idea and designed the experiments. S. V. grew the STO films. M. R. grew the $SrCa_2Al_2O_6$ films under the supervision of M. C. S. V. transferred membranes and performed the structural characterization. S. V. and S. C. performed the electrical measurements. S. V., M. C. and B. J. wrote the manuscript. All authors contributed to the discussion and manuscript preparation. B. J. directed the overall aspects of the project.

Data availability

The authors confirm that all the data required to conclude the findings of this study have been included in the ESI.†

Conflicts of interest

There are no conflicts to declare.

Acknowledgements

Synthesis of the membrane and characterization (S. V. and B. J.) were supported by the U. S. Department of Energy through DE-SC0020211. Device characterization (fabrication and dielectric measurements) was supported as part of the Center for Programmable Energy Catalysis, an Energy Frontier Research Center funded by the U. S. Department of Energy, Office of Science, Basic Energy Sciences at the University of Minnesota, under Award No. DE-SC0023464. S. C. acknowledges support from the Air Force Office of Scientific Research (AFOSR) through Grant No. FA9550-21-1-0025 and FA9550-21-0460. Film growth was performed using instrumentations funded by AFOSR DURIP awards FA9550-18-1-0294 and FA9550-23-1-0085. Parts of this work were carried out at the Characterization Facility, University of Minnesota, which receives partial support from the NSF through the MRSEC program under award DMR-2011401. Exfoliation of films and device fabrication were carried out at the Minnesota Nano Center, which is supported by the NSF through the National Nano Coordinated Infrastructure under award ECCS-2025124. M. C. acknowledges funding by MICIN PID2020-114224RB-I00/AEI/10.13039/501100011033. The work of M. R. has been performed in the framework of the doctorate in Materials Science of the Autonomous University of Barcelona.

References

1 N. Pryds, D.-S. Park, T. S. Jespersen and S. Yun, *APL Mater.*, 2024, **12**, 010901.
2 J. A. Rogers, M. G. Lagally and R. G. Nuzzo, *Nature*, 2011, **477**, 45–53.
3 P.-C. Wu and Y.-H. Chu, *J. Mater. Chem. C*, 2018, **6**, 6102–6117.
4 M. Yao, Y. Cheng, Z. Zhou and M. Liu, *J. Mater. Chem. C*, 2020, **8**, 14–27.
5 Y. Bitla and Y.-H. Chu, *Nanoscale*, 2020, **12**, 18523–18544.
6 A. G. Ricciardulli, S. Yang, J. H. Smet and M. Saliba, *Nat. Mater.*, 2021, **20**, 1325–1336.
7 O. Dubnack and F. A. Müller, *Materials*, 2021, **14**, 5213.
8 H. Yoon, T. K. Truttmann, F. Liu, B. E. Matthews, S. Choo, Q. Su, V. Saraswat, S. Manzo, M. S. Arnold, M. E. Bowden, J. K. Kawasaki, S. J. Koester, S. R. Spurgeon, S. A. Chambers and B. Jalan, *Sci. Adv.*, 2022, **8**, eadd5328.
9 S. S. Hong, M. Gu, M. Verma, V. Harbola, B. Y. Wang, D. Lu, A. Vailionis, Y. Hikita, R. Pentcheva, J. M. Rondinelli and H. Y. Hwang, *Science*, 2020, **368**, 71–76.
10 S. S. Hong, J. H. Yu, D. Lu, A. F. Marshall, Y. Hikita, Y. Cui and H. Y. Hwang, *Sci. Adv.*, 2017, **3**, eaao5173.
11 J.-K. Huang, Y. Wan, J. Shi, J. Zhang, Z. Wang, W. Wang, N. Yang, Y. Liu, C.-H. Lin, X. Guan, L. Hu, Z.-L. Yang, B.-C. Huang, Y.-P. Chiu, J. Yang, V. Tung, D. Wang, K. Kalantar-Zadeh, T. Wu, X. Zu, L. Qiao, L.-J. Li and S. Li, *Nature*, 2022, **605**, 262–267.
12 J. Ji, S. Park, H. Do and H. S. Kum, *Phys. Scr.*, 2023, **98**, 052002.
13 K. Kerman and S. Ramanathan, *J. Mater. Res.*, 2014, **29**, 320–337.
14 D. Pesquera, A. Fernández, E. Khestanova and L. W. Martin, *J. Phys.: Condens. Matter*, 2022, **34**, 383001.
15 S. R. Bakaul, C. R. Serrao, M. Lee, C. W. Yeung, A. Sarker, S.-L. Hsu, A. K. Yadav, L. Dedon, L. You, A. I. Khan, J. D. Clarkson, C. Hu, R. Ramesh and S. Salahuddin, *Nat. Commun.*, 2016, **7**, 10547.

16 D. Lu, D. J. Baek, S. S. Hong, L. F. Kourkoutis, Y. Hikita and H. Y. Hwang, *Nat. Mater*, 2016, **15**, 1255–1260.
17 D. Pesquera, E. Khestanova, M. Ghidini, S. Zhang, A. P. Rooney, F. Maccherozzi, P. Riego, S. Farokhipoor, J. Kim, X. Moya, M. E. Vickers, N. A. Stelmashenko, S. J. Haigh, S. S. Dhesi and N. D. Mathur, *Nat. Commun.*, 2020, **11**, 3190.
18 W. Zhou, W. Han, Y. Yang, L. Shu, Q. Luo, Y. Ji, C. Jin, Y. Zhang, J. Song, M. Ye, Q. Liu, S. Hu and L. Chen, *Appl. Phys. Lett.*, 2023, **122**, 062901.
19 K. Han, L. Wu, Y. Cao, H. Wang, C. Ye, K. Huang, M. Motapothula, H. Xing, X. Li, D.-C. Qi, X. Li and X. Renshaw Wang, *ACS Appl. Mater. Interfaces*, 2021, **13**, 16688–16693.
20 H. Peng, N. Lu, S. Yang, Y. Lyu, Z. Liu, Y. Bu, S. Shen, M. Li, Z. Li, L. Gao, S. Lu, M. Wang, H. Cao, H. Zhou, P. Gao, H. Chen and P. Yu, *Adv. Funct. Mater.*, 2022, **32**, 2111907.
21 Y.-W. Chang, P.-C. Wu, J.-B. Yi, Y.-C. Liu, Y. Chou, Y.-C. Chou and J.-C. Yang, *Nanoscale Res. Lett.*, 2020, **15**, 172.
22 P. Singh, A. Swartz, D. Lu, S. S. Hong, K. Lee, A. F. Marshall, K. Nishio, Y. Hikita and H. Y. Hwang, *ACS Appl. Electron. Mater.*, 2019, **1**, 1269–1274.
23 P. Salles, I. Caño, R. Guzman, C. Dore, A. Mihi, W. Zhou and M. Coll, *Adv. Mater. Inter*, 2021, **8**, 2001643.
24 P. Salles, R. Guzman, A. Barrera, M. Ramis, J. M. Caicedo, A. Palau, W. Zhou and M. Coll, *Adv. Funct. Mater.*, 2023, **33**, 2304059.
25 R. W. Schwartz, T. Schneller and R. Waser, *C. R. Chim*, 2004, **7**, 433–461.
26 M. Coll and M. Napari, *APL Mater.*, 2019, **7**, 110901.
27 A. J. M. Mackus, J. R. Schneider, C. MacIsaac, J. G. Baker and S. F. Bent, *Chem. Mater.*, 2019, **31**, 1142–1183.
28 X. Obradors, T. Puig, A. Pomar, F. Sandiumenge, S. Piñol, N. Mestres, O. Castaño, M. Coll, A. Cavallaro, A. Palau, J. Gázquez, J. C. González, J. Gutiérrez, N. Romà, S. Ricart, J. M. Moretó, M. D. Rossell and G. V. Tendeloo, *Supercond. Sci. Technol.*, 2004, **17**, 1055–1064.
29 S. Varshney, S. Choo, L. Thompson, Z. Yang, J. Shah, J. Wen, S. J. Koester, K. A. Mkhoyan, A. S. McLeod and B. Jalan, *ACS Nano*, 2024, **18**, 6348–6358.
30 W. Nunn, T. K. Truttmann and B. Jalan, *J. Mater. Res.*, 2021, **36**, 4846–4864.
31 S. Jesse, A. P. Baddorf and S. V. Kalinin, *Appl. Phys. Lett.*, 2006, **88**, 062908.
32 P. Salles, R. Guzmán, D. Zanders, A. Quintana, I. Fina, F. Sánchez, W. Zhou, A. Devi and M. Coll, *ACS Appl. Mater. Interfaces*, 2022, **14**, 12845–12854.
33 B. Jalan, P. Moetakef and S. Stemmer, *Appl. Phys. Lett.*, 2009, **95**, 032906.
34 J. Yue, Y. Ayino, T. K. Truttmann, M. N. Gastiasoro, E. Persky, A. Khanukov, D. Lee, L. R. Thoutam, B. Kalisky, R. M. Fernandes, V. S. Pribiag and B. Jalan, *Sci. Adv.*, 2022, **8**, eabl5668.
35 H. W. Jang, A. Kumar, S. Denev, M. D. Biegalski, P. Maksymovych, C. W. Bark, C. T. Nelson, C. M. Folkman, S. H. Baek, N. Balke, C. M. Brooks, D. A. Tenne, D. G. Schlom, L. Q. Chen, X. Q. Pan, S. V. Kalinin, V. Gopalan and C. B. Eom, *Phys. Rev. Lett.*, 2010, **104**, 197601.
36 K. T. Kang, H. I. Seo, O. Kwon, K. Lee, J.-S. Bae, M.-W. Chu, S. C. Chae, Y. Kim and W. S. Choi, *Appl. Surf. Sci.*, 2020, **499**, 143930.
37 Y. S. Kim, J. Kim, S. J. Moon, W. S. Choi, Y. J. Chang, J.-G. Yoon, J. Yu, J.-S. Chung and T. W. Noh, *Appl. Phys. Lett.*, 2009, **94**, 202906.
38 H. Uwe and T. Sakudo, *Phys. Rev. B: Condens. Matter Mater. Phys.*, 1976, **13**, 271–286.
39 M. Guennou, P. Bouvier, J. Kreisel and D. Machon, *Phys. Rev. B: Condens. Matter Mater. Phys.*, 2010, **81**, 054115.
40 R. Loetzsch, A. Lübcke, I. Uschmann, E. Förster, V. Große, M. Thuerk, T. Koettig, F. Schmidl and P. Seidel, *Appl. Phys. Lett.*, 2010, **96**, 071901.
41 M. Itoh, R. Wang, Y. Inaguma, T. Yamaguchi, Y.-J. Shan and T. Nakamura, *Phys. Rev. Lett.*, 1999, **82**, 3540–3543.
42 W. Peng, R. Tétot, G. Niu, E. Amzallag, B. Vilquin, J.-B. Brubach and P. Roy, *Sci. Rep.*, 2017, **7**, 2160.
43 Y. Zhang, J. Li, K. Yang, F. Zheng, Y. Zhou, Y. Zhang, Y. Hui, Y.-Q. Wang, J. Zhu, J. Zhang, Y. Hao, M. Yang, T. Li, J. Zhao and H. H. Ma, *APL Mater.*, 2023, **11**, 041103.